How Coalescing Droplets Jump

Ryan Enright,[†,‡,#,*] Nenad Miljkovic,[‡,§] James Sprittles,[⊥] Kevin Nolan,[†] Robert Mitchell,[∥,▽] and Evelyn N. Wang[‡,*]

[†]Thermal Management Research Group, Efficient Energy Transfer (ηET) Department, Bell Laboratories Ireland, Alcatel-Lucent Ireland Ltd., Blanchardstown Business & Technology Park, Snugborough Road. Dublin 15, Ireland, [‡]Department of Mechanical Engineering, Massachusetts Institute of Technology, 77 Massachusetts Avenue, Cambridge, Massachusetts 02139, United States, [§]Department of Mechanical Science and Engineering, University of Illinois, Urbana, Illinois 61801, United States, [⊥]Mathematics Institute, University of Warwick, Coventry CV4 7AL, United Kingdom, [∥]Department of Materials Science and Engineering, Massachusetts Institute of Technology, 77 Massachusetts Avenue, Cambridge, Massachusetts 02139, United States, and [#]Stokes Institute, University of Limerick, Limerick Ireland [▽]Present address: Intel Corp., 5200 NE Elam Young Parkway, m/s RA3-301, Hillsboro, Oregon 97124, USA.

ABSTRACT Surface engineering at the nanoscale is a rapidly developing field that promises to impact a range of applications including energy production, water desalination, self-cleaning and anti-icing surfaces, thermal management of electronics, microfluidic platforms, and environmental pollution control. As the area advances, more detailed insights of dynamic wetting interactions on these surfaces are needed. In particular, the coalescence of two or more droplets on ultra-low adhesion surfaces leads to droplet jumping. Here we show, through detailed measurements of jumping droplets during water condensation coupled with numerical simulations of binary droplet coalescence, that this process is fundamentally inefficient with only a small fraction of the available excess surface energy ($\lesssim$6%) convertible into translational kinetic energy. These findings clarify the role of internal fluid dynamics during the jumping droplet coalescence process and underpin the development of systems that can harness jumping droplets for a wide range of applications.

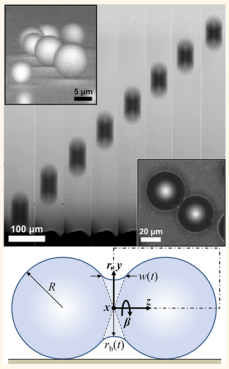

KEYWORDS: nanostructured surface design · coalescence · droplet jumping · microfluidics · condensation · wetting · superhydrophobic

When two or more droplets coalesce on a ultra-low adhesion nanostructured surface, the resulting droplet can jump away from the surface in a process that has been termed "coalescence-induced droplet jumping".[1−6] Droplet jumping has recently received significant attention due its fundamental relevance in understanding dynamic droplet processes,[7−19] evolved surface structures found in nature,[20] and surface-charge separation.[3] Jumping droplets have also been used to enhance performance in a variety of applications including condensation heat transfer,[2,21−23] self-cleaning surfaces,[24] thermal diodes,[25,26] anti-icing surfaces,[6,27,28] and energy harvesting.[29] Beyond these demonstrated applications, droplet jumping also has potential for use in thermally driven water desalination systems,[30] in combination with acoustophoretic droplet manipulation to realize novel microfluidic platforms[31] and in mitigating environmentally polluting gas and particle emissions by providing a convenient waste-heat-driven source of microscopic water droplets for wet scrubbing systems.[32]

At the basic level, droplet jumping is a process governed by the conversion of excess surface energy into kinetic energy when two or more droplets coalesce[7,33] and involves a symmetry-breaking surface.[8] For the simplest case of two, equally sized inviscid spherical droplets coalescing on a surface with no adhesion, an energy-balance gives a characteristic jumping speed that follows an inertial-capillary scaling[7]

$$U \sim \sqrt{\gamma/\rho R} \qquad (1)$$

where R, γ, and ρ are the initial radii, surface tension, and density of the droplets, respectively. Previous water condensation experiments on a hierarchical superhydrophobic surface have shown an approximately constant scaled jumping speed of $\approx 0.2U$ for jumping droplets with diameters larger than $\approx$100 μm. For smaller diameters, jumping speeds rapidly decreased with no droplet jumping observed below diameters of $\approx$20 μm.[7] Several subsequent studies have attempted to explain these observations by adding terms to the energy-balance approach to account for viscous dissipation, surface adhesion effects and participating velocity components,[9,13,16] but have demonstrated

* Address correspondence to ryan.enright@alcatel-lucent.com, enwang@mit.edu.

Received for review July 4, 2014 and accepted August 29, 2014.

Published online August 29, 2014
10.1021/nn503643m

limited success. While a recent numerical simulation replicated experimental observations,[1] this study was limited to a single droplet diameter. Despite the significant research efforts, there continues to be a lack of quantitative experimental data characterizing droplet jumping and the precise mechanism governing droplet jumping remains not well-understood.

In this work, we studied the process of coalescence-induced droplet jumping over a wide parameter space using a combination of water condensation experiments on nanostructured superhydrophobic surfaces and detailed numerical simulations. To experimentally isolate the fundamental energy conversion process associated with droplet jumping, we fabricated surfaces demonstrating *apparent* contact angles approaching 180° and almost zero contact angle hysteresis, thus mitigating the influence of surface adhesion.[4,11] Using high-speed imaging, we measured droplet-jumping speeds normal to the condensing surface as high as 1.4 m/s for jumping droplet diameters as small as ≈10 μm. However, while the measured velocities were up to approximately six times larger than the highest velocities previously reported,[7,9] they were still approximately one-fifth of the speed indicated by eq 1.

Meanwhile, using 2D axisymmetric numerical simulations, we obtained detailed information on the internal flow momentum generated during droplet coalescence. By recognizing that only unbalanced momentum components can contribute to droplet translational motion, a fact neglected in the derivation of eq 1, we found that coalescence-induced droplet jumping is an inherently *inefficient* process with only a small fraction of the available excess surface energy ΔE ($\lesssim$6%) being converted to *useful* internal flow momentum to provide the jumping droplet with translational kinetic energy E_j, *i.e.*, $\eta_j = E_j/\Delta E \lesssim 0.06$. Contrary to previous conclusions drawn from theoretical estimates,[9,13] we found that internal viscous dissipation plays a limited role in the jumping process for the experimentally accessible low *Oh* number regime studied ($Oh = \mu/(\rho\gamma R)^{1/2} \lesssim 0.1$, where μ is the droplet dynamic viscosity).[34] With our developed understanding, we determined a dimensionless droplet-size-dependent correction to eq 1 that demonstrated good agreement with our experimental data. Our results elucidate the coupled nature of surface-mediated symmetry breaking and the internal flow momentum on jumping droplet dynamics. Furthermore, our mechanistic framework provides a starting point for more detailed analysis involving complicating factors such as finite surface adhesion, unequal coalescing droplet geometries and complex surface architectures.

RESULTS AND DISCUSSION

Experiments. To minimize the influence of the underlying substrate on the droplet jumping process, we prepared fluoropolymer-coated carbon nanotube (CNT)-based superhydrophobic surfaces with a

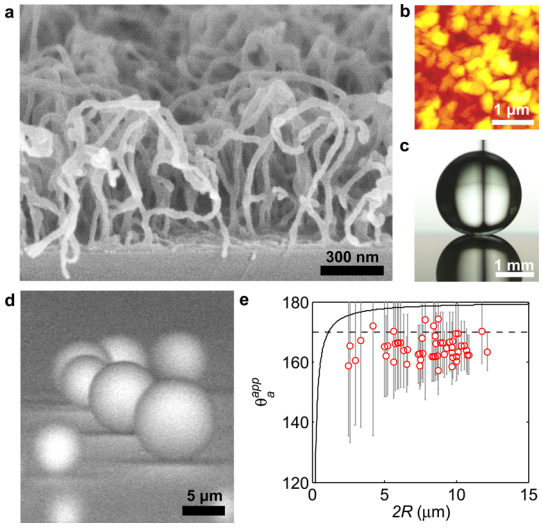

Figure 1. Hydrophobic CNT turf. (a) SEM image of CNT surface with P2i hydrophobic coating. (b) AFM scan in soft-tapping mode of the P2i-coated CNT surface. The scan revealed a maximum height variation of ~820 nm consistent with the height measured from SEM images. (c) Macroscopic droplet in the receding state on the P2i-coated CNT surface (θ_r^{app} = 166° ± 2°). (d) ESEM image of condensed droplets taken at an inclination angle of 8° from the horizontal plane. (e) Advancing contact angles on the P2i-coated CNT turf measured from the ESEM images (open circles). The solid curve is defined by $\theta_{app} = \cos^{-1}(r_p/R) + 90°$ with a conservatively estimated pinned base radius under the droplet of r_p = 100 nm. The horizontal dashed line represents the macroscopically measured advancing apparent contact angle, θ_a^{app} = 170.2° ± 2.4°.

structure spacing length scale of $l \sim 100$ nm that was much smaller than the typical jumping droplet radius ($l/R \sim 0.01 \ll 1$) (see Methods). The coated CNTs had typical diameters of $d \approx 40$ nm (Figure 1a) and atomic force microscopy scans of the surface in soft tapping mode showed a maximum height variation of 820 nm, consistent with the height measured from scanning electron microscope images of the surface (Figure 1b). Measurements of the advancing macroscopic contact angle demonstrated highly nonwetting behavior, θ_a^{app} = 170.2°($\cos\theta_a^{app} = -0.985 \approx -1$) (Figure 1c). Moreover, the measured contact angle hysteresis of macroscopic droplets was found to be small ($\Delta \cos\theta = \cos\theta_a^{app} - \cos\theta_r^{app} = -0.0154 \approx 0$). Condensed droplets with diameters as small as 2 μm demonstrated large apparent contact angles (Figure 1d) similar to the macroscopically measured value (Figure 1e). A conservative estimate of the droplet radius-dependent advancing angle, $\theta_a^{app}(R)$, indicated that all measured droplet jumping events were in a constant contact angle growth mode.[4] We also fabricated and tested fluoropolymer-coated CuO nanostructures, which we have previously shown to demonstrate good jumping droplet behavior,[2−4] with macroscopic advancing contact angle and contact angle hysteresis behavior similar to that of the functionalized CNT surfaces (see Methods). Since the characteristic roughness spacing length scales of the surfaces

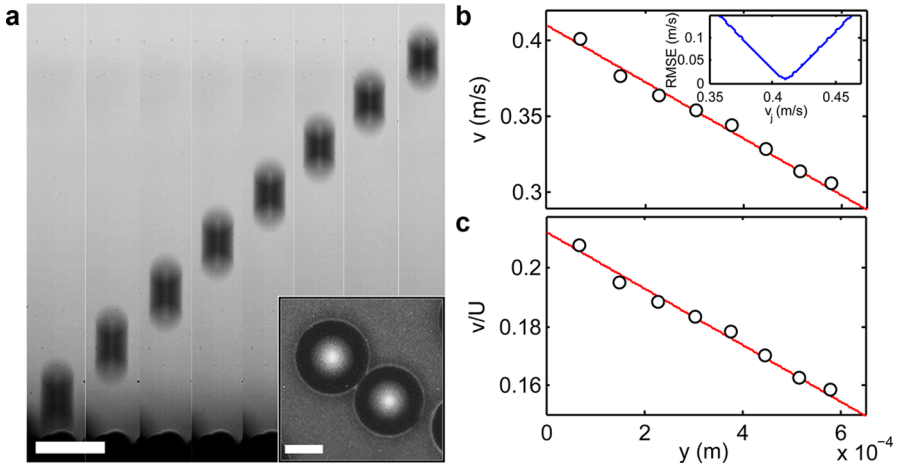

Figure 2. Jumping droplet trajectory. (a) High-speed time-lapse images capturing coalescence-induced droplet jumping (wall temperature, T_w = 5 °C, water vapor pressure, p_v = 0.87 kPa). Shutter speed: 185 μs. Scale bar: 100 μm. Inset: Overhead view of droplets prior to jumping where R_1 = 20.2 μm (left) and R_2 = 19 μm (right) (R_j = 24.7 μm). Scale bar: 20 μm. (b) Droplet velocity as a function of height above the surface. The line shows the fitted trajectory given by Supporting Information eq S1, indicating a jumping velocity of v_j = 0.41 ± 0.01 m/s. Inset: Root mean square error (RMSE) of the fit of Supporting Information eq S1 to the measured velocities. The estimated jumping velocity was evaluated at the minima of the calculated RMSE. (c) Jumping velocity in (b) scaled by the characteristic speed given by eq 1, indicating v_j/U = 0.21 ± 0.01.

($l \approx 0.1-1$ μm) were significantly smaller than the smallest droplet jumping diameter measured (≈10 μm), we were able access a droplet growth regime well above the flooding limit with droplets growing in a constant *apparent* contact angle mode.[2,4,5] Since the work of adhesion scales as $W \propto (1 + \cos\theta)$, the contact angle measurements suggested that the effect of surface adhesion on the droplet jumping process could be neglected.

Condensation experiments were carried out under humid atmospheric conditions using a two-camera arrangement and in a pressure-regulated environmental chamber using a single-camera arrangement (see Methods, Supporting Information S2−S4). In the former experimental setup, an overhead CCD camera was used to capture images of the droplets prior to coalescence to provide the initial conditions, *i.e.*, the droplet radii and number of droplets involved in the jumping event. Knowledge of these initial conditions allowed us to isolate binary droplet jumping events for droplets of equal radii with near surface-normal trajectories that maximized the jumping velocity.[7,11] The latter experimental setup allowed us to study droplet jumping at condensing surface temperatures higher than the laboratory ambient conditions and under varying gas densities to rule out the possibility that external drag plays a significant role during the droplet coalescence process before jumping, as assumed in our numerical simulations. In both experimental setups, a high-speed camera was used to capture the out-of-plane jumping droplet trajectory.

Figure 2a shows representative time-lapse images capturing a jumping droplet following the coalescence of two equally sized droplets ($R \approx 19.5$ μm) obtained using the two-camera arrangement. The center of the streak was taken as the average y position of the jumping droplet in each frame relative to the initial location of the droplets on the condensing surface (y = 0), while the average velocity of the jumping droplet was found by measuring the length of the streak and dividing this by the shutter speed of the camera. These two measures together defined the experimental trajectory of the jumping droplets. To obtain an accurate estimate of the jumping velocity associated with the converted excess surface energy, the theoretical droplet trajectory was calculated (see Supporting Information S5).

In Figure 2b, the theoretical trajectory is shown fitted to the experimental data to determine the droplet jumping velocity as it departed the surface. On the basis of the fitted trajectory, we determined a jumping velocity of v_j = 0.41 ± 0.01 m/s (inset of Figure 2b), which was 0.21× the characteristic jumping speed given by the capillary-inertial scaling, $U \approx [\gamma/(\rho R)]^{1/2}$ = 1.92 m/s (Figure 2c). This result was generally repeatable over a number of experiments for a wide range of droplet sizes and is consistent with the previously identified size-independent region.[7] To better understand the reason for jumping velocity magnitudes significantly smaller than those given by eq 1 in view of the ultra-low surface adhesion characteristic of the condensing surfaces in our study, we considered the nature of the droplet coalescence process and performed numerical simulations to determine the jumping velocity in the absence of surface adhesion effects. Analysis of the simulations improved our understanding of how the excess surface energy was transferred to the translational kinetic energy of the jumping droplet by considering the details of the internal flow developed during the coalescence process.

Theory and Simulations. A schematic of the coalescence process for two, equally sized, condensed

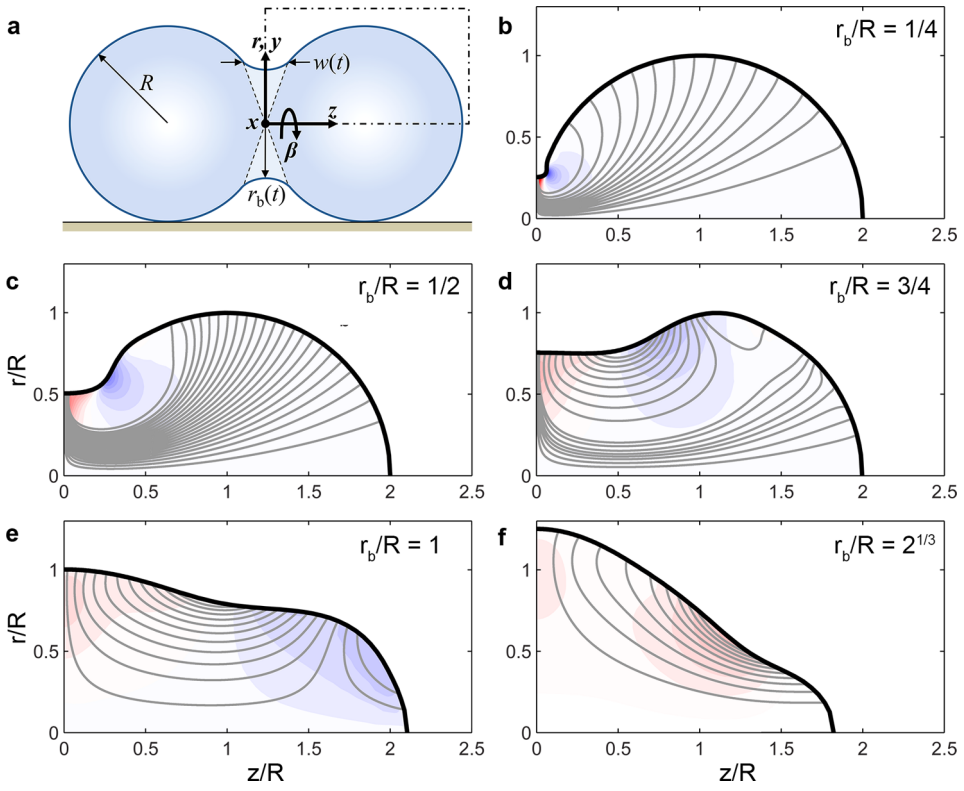

Figure 3. Internal flow field during droplet coalescence. (a) Schematic of two condensed droplets undergoing coalescence defined by an initial radius R, a time-varying capillary bridge radius r_b, and a time-varying capillary bridge width $w = r_b^2/R$ on a superhydrophobic surface characterized by $\theta_a^{app} \rightarrow 180°$. A cylindrical coordinate system (r, z, β) is defined with the origin at the point where the two droplets meet. The z-coordinate is parallel to the surface, while the radial r-coordinate is resolved into y- and x-coordinates at $\beta = \pi/2$ (pointed to the top of the page) and $\beta = 0$ (pointed into the page), respectively. (b−f) Numerically simulated flow field of the coalescence process for $Oh = 0.012$ ($R = 100\ \mu$m) and $1/4 < r_b/R \leq 2^{1/3}$ in the region of the droplet indicated by the dot-dashed box in (a). Simulated fluid properties: $\gamma = 72 \times 10^{-3}$ N/m, $\rho = 1 \times 10^3$ kg/m^3, $\mu = 1 \times 10^{-3}$ Pa·s. The contours depict the radial velocity component with red and blue coloring indicating flow away and toward the z-axis, respectively. The gray lines depict the streamlines of the flow. At the earlier stage of coalescence (b), the generated radial flow is restricted primarily to the local bridge region ($z/R = 0$). This flow is fed by a region of negative radial flow that can be clearly seen in (c) due to the differences in the local curvature along the droplet interface. In (d), the positive and negative radial flow regions expand as the capillary wave moves away from the bridge region. In (e), the negative radial flow feeding the positive radial flow centered around $z/R = 0$ has arrived at the edge of the droplet. (f) The negative radial flow has vanished and the entire upper portion of the droplet has a positive radial velocity driven by the curvature difference between the interface at $z/R \approx 1.75$ ($r/R \approx 0$) and $z/R \approx 0$ ($r/R \approx 2^{1/3}$).

droplets defined by a radius, R, resting on a surface characterized by $\theta_a^{app} \rightarrow 180°$ and $\Delta \cos\theta \rightarrow 0$ is shown in Figure 3a. Soon after the interfaces of the two droplets make contact, a liquid bridge develops that is accelerated radially from the point of contact due to the curvature difference (in the longitudinal direction) between the bridge radius ($1/r_b$) and the droplets ($1/R$). Initially, viscous forces control the bridge flow dynamics. However, inertia begins to dominate the flow dynamics when the bridge radius, r_b, exceeds the critical bridge radius $r_c = 64\,\mu^2/(\rho\gamma C^4)$,[34,35] where C is a constant previously determined from simulation[36] and experimental measurement[35,37,38] to have a value ranging between 1.39 and 1.62. For water at ambient conditions and based on the range of C, $r_c \approx$ 165−311 nm. Considering the inertial regime, scaling of the bridge flow yields a time-varying bridge radius $r_b(t)$ formed during coalescence given by[36,39]

$$r_b = CR\sqrt{t/\tau} \tag{2}$$

where $\tau = (\rho R^3/\gamma)^{1/2}$ is the inertial-based time scale of the coalescence process. Differentiating eq 2 with respect to time gives

$$v_b = \frac{1}{2}\frac{CR}{\sqrt{\tau t}} \tag{3}$$

Noting the definition of τ, eq 3 shows that $v_b \sim (\gamma/\rho R)^{1/2}$, corresponding to the scaling given by eq 1. This equivalence between the energy state scaling and the scaling behavior of the radial bridging flow highlights the link between the jumping droplet speed and the excess surface energy being transferred to the internal flow during the coalescence process. Specifically, by considering the symmetry of the system, we seek to relate the internal flow to the jumping of the droplet from the surface by finding the momentum component of the internal flow normal to the symmetry-breaking surface, *i.e.*, y-coordinate in Figure 3a. Due to symmetry considerations, the other two momentum components parallel to the surface (x- and z-coordinates)

give zero net momentum before and after the impact of the bridging flow on the surface.

To determine the *y*-component of momentum, p_y, generated during the coalescence process, 2D axisymmetric numerical simulations were performed using a finite-element code specifically designed to accurately model unsteady microcapillary flows in which both viscous and inertial forces are present in the liquid. This code has previously been shown to accurately capture the coalescence process,[40] and was originally developed for dynamic wetting flows[41] (see Methods).

In Figure 3b−f, the numerically simulated flow field of the coalescence process for $Oh = 0.012 (r_c/R = 64Oh^2/C^4 \approx 2 \times 10^{-3})$, corresponding to water droplets at approximately ambient conditions with initial radii of $R = 100\ \mu$m, and $0.25 \leq r_b/R \leq 2^{1/3}$ is shown in terms of the radial velocity component, u_r, and the flow streamlines (see Supporting Information S6 for flow fields obtained for larger *Oh*). In the early stages of coalescence (r_b/R = 1/4), flow enters the expanding liquid bridge from the droplet bulk near the bridge due to the low pressure region generated by the large longitudinal bridge curvature.[39] The bridging process generates a capillary wave (Figure 4a) that propagates along the interface away from the bridge region. The local pressures associated with the capillary wave fluctuate above and below the initial equilibrium pressure. As the capillary wave propagates and disperses (Figure 4b-d), there is a corresponding expansion in both the positive and negative components of the radial velocity (Figure 3c−e). Beyond r_b/R = 1, the negative radial flow decays until, at $r_b/R = 2^{1/3}$ (Figure 3f), the radial flow component is positive everywhere. This result corresponds to a relatively large pressure fluctuation as the capillary wave reaches the end of the droplet and is reflected back toward the coalescence symmetry plane. This increase in pressure, as well as the inertia already obtained, generates a flow with a significant positive radial component (Figure 3f).

Also shown in Figure 4 are the capillary wave characteristics for larger *Oh* values of $0.037 (r_c/R \approx 2 \times 10^{-2})$ and 0.118 ($r_c/R \approx 0.13-0.24$). As *Oh* increases, the propagating capillary wave driving the internal flow becomes significantly damped, a consequence of the *Oh* number representing the dimensionless viscosity. The reduced amplitude of the pressure fluctuations with respect to the initial equilibrium pressure along with increased viscous dissipation within the droplet leads to a characteristic change in both the interface shape evolution and internal flow field of the coalescing droplet (see Supporting Information S6). As we show later, this behavior correlates with the magnitude of the internal flow momentum generated during coalescence to give an *Oh*-dependent jumping velocity.

The change in droplet shape evolution and internal flow field was reflected in the cumulative viscous dissipation of the flow during the coalescence process,

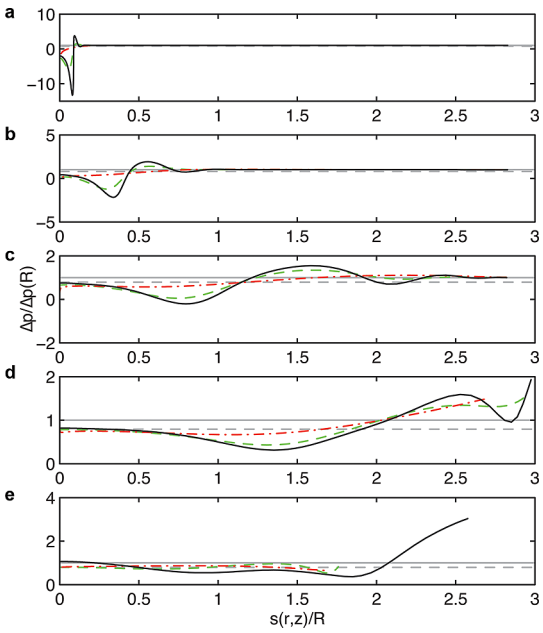

Figure 4. Capillary wave during droplet coalescence. Pressure profiles at the liquid/vapor interface along the normalized interface position, *s*(*r*,*z*)/*R*. The pressure difference across the interface is normalized by the initial equilibrium pressure of the two droplets, $\Delta p(R) = 2\gamma/R$. The light horizontal solid line and dashed line correspond to $\Delta p/\Delta p(R) = 1$ and $\Delta p(2^{1/3}R)/\Delta p(R) \approx 0.8$, respectively. The solid curve (black) depicts the pressure profiles obtained for *Oh* = 0.012 corresponding to the flow fields shown in Figure 3. The dashed (green) and dash-dot (red) curves depict the pressure profiles obtained for *Oh* = 0.037 and *Oh* = 0.118, respectively.

$E_d(r_b/R)$, normalized by the available excess surface energy budget, ΔE, shown in Figure 5a. As expected, an increasing proportion of the excess surface energy budget was consumed by viscous losses with increasing *Oh*. Figure 5b shows the normalized viscous dissipation evaluated from our simulations at $r_b/R = 2^{1/3}$ as a function of *Oh* and previous estimations.[9,13] The dissipation estimates are seen to either under-predict or over-predict the viscous losses compared to our simulations. More importantly though, both previous estimates predict a linear increase in viscous dissipation with increasing *Oh*, which is due to the fact that only a single inertial time scale was used to characterize droplet coalescence for all *Oh*.[9,13] The simulation results, however, show a decreasing rate of viscous dissipation growth with increasing *Oh*. This can be understood by considering the limiting case of a very large *Oh* where the normalized viscous dissipation must asymptote to unity when evaluated up to $r_b/R = 2^{1/3}$ resulting in a smooth transition to a sphere during coalescence.[40] As we show next, simply adding a viscous dissipation term into the energy-balance analysis cannot capture the subtle effect of viscosity on the development of the internal flow momentum component normal to the condensing surface with varying *Oh*.

To extract the *y*-component (surface-normal) of momentum from the simulations, we considered

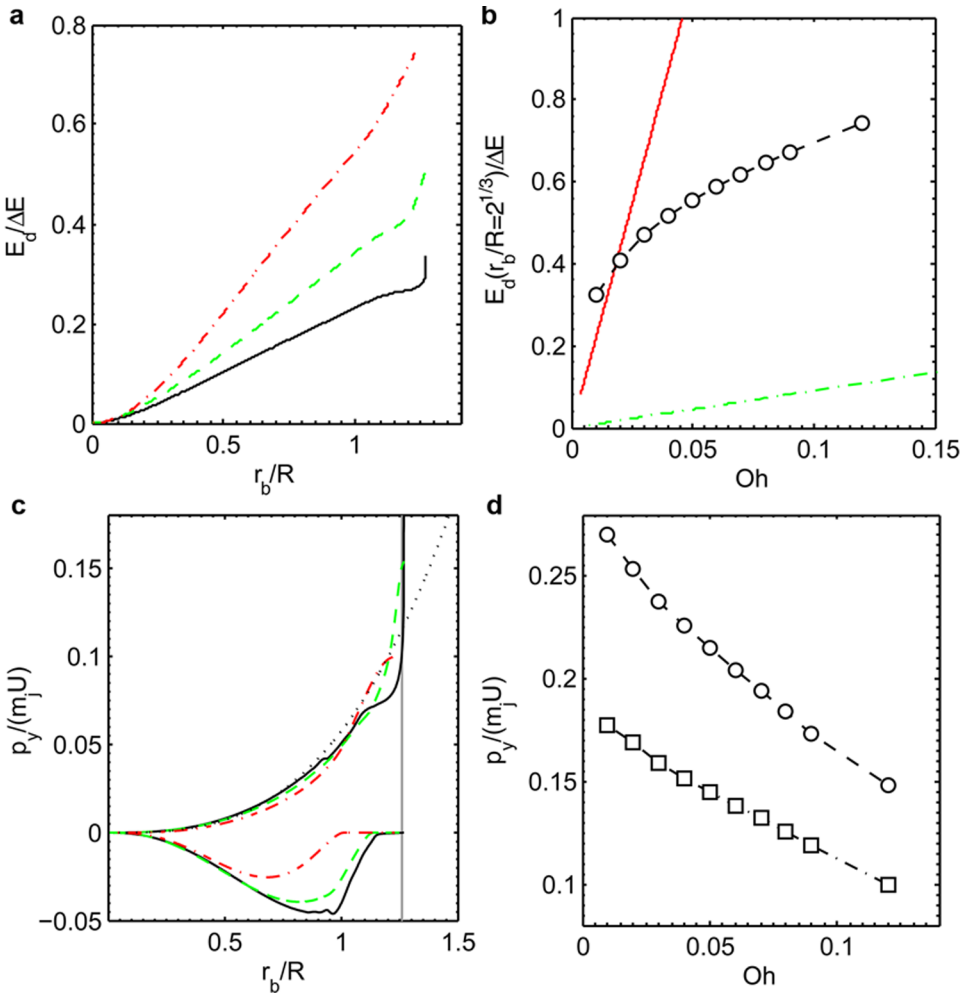

Figure 5. Viscous dissipation and momentum generation. (a) Viscously dissipated energy scaled by the excess surface energy budget during the coalescence process up to $r_b/R = 2^{1/3}$ for *Oh* = 0.012 (solid curve), *Oh* = 0.037 (dashed curve) and *Oh* = 0.118 μm (dot-dashed curve). (b) Viscously dissipated energy at $r_b/R = 2^{1/3}$ (circles) scaled by the excess surface energy budget as a function of the *Oh* number. The dashed and dot-dashed lines correspond to the viscous dissipation terms estimated in refs 13 and 9, respectively. (c) Numerically simulated positive and negative momentum *y*-components ($y > 0$) scaled by the characteristic momentum as a function of the bridge radius for *Oh* = 0.012 (solid curve), *Oh* = 0.037 (dashed curve) and *Oh* = 0.118 μm (dot-dashed curve). The dashed line corresponds to eq 5 with $C = 1.3$. The vertical solid line corresponds to $r_b/R = 2^{1/3}$. The simple inertial model of the bridging phase (dot curve) shows good agreement with the low *Oh* number data up to $r_b/R \approx 1$. For increasing *Oh* number, we observe a deviation from the simple inertial model. (d) Maximum value of the dimensionless *y*-component momentum in the upper portion of the droplets $p_y^+|_{\max(r_b/R \geq 2^{1/3})}/(m_jU)$ contributing to the droplet jumping velocity as a function of *Oh* number (squares). Sum of the dimensionless *y*-component momentum contributions $\Sigma p_y/(m_jU)$ to the droplet jumping velocity given by eq 6 as a function of *Oh* number (circles). Both the *y*-component momentum in the upper portion of the droplets and the total momentum scale approximately as $-Oh$.

axisymmetric motion about the *z*-axis of a cylindrical coordinate system (r, z, β) for $z > 0$ due to the symmetry between the two coalescing drops. The velocity component perpendicular to the surface is $u_y = u_r \sin \beta$, where u_r is the velocity in the radial direction and β is the azimuthal coordinate. Accordingly, the momentum perpendicular to the surface in the *upper half* of the two coalescing droplets is

$$p_y = 2\rho \iint_0^{\pi} r u_r \sin\beta \, d\beta dr dz \qquad (4)$$

The first integral in eq 4 gives the *y*-component of the radial velocity, while the second integral operates over the $r-z$ plane. The total momentum given by eq 4 can be further broken down into positive, p_y^+, and negative, p_y^-, contributions to p_y depending on whether the associated radial flow is moving away from or toward the *z*-axis.

Figure 5c shows the *y*-components of the momentum extracted from the numerical simulations nondimensionalised by the characteristic momentum of the system, m_jU, for *Oh* = 0.012, 0.037, and 0.118. The results are compared to the prediction of a simple model description of the *y*-component of the bridging flow momentum in the inertial limit (see Supporting Information S7 for derivation) given by

$$\frac{p_y^+|_{r_b/R \lesssim 1}}{m_jU} = \frac{3}{2\pi} C^2 \left(\frac{r_b}{R}\right)^3 \qquad (5)$$

Despite the simplified nature of our analysis, we find that a numerical prefactor of $C = 1.3$ inserted into eq 5 provides good agreement with the simulated p_y^+ up to $r_b/R \approx 1$ for the smallest simulated *Oh*. This serves to highlight the dominant role of the bridging flow in generating internal flow momentum at this stage of the coalescence process.

For $Oh = 0.012$ and $r_b/R \gtrsim 1$, we observed a distinct reduction in the growth of the numerically simulated p_y^+ coinciding with positive radial flow spreading to the entire droplet and the commensurate decay of the negative radial flow (Figure 3e,f) that can be observed in Figure 5c in terms of the negative momentum, p_y^-, that reached a minimum at $r_b/R \approx 1$ before returning to zero. The dwell in the positive momentum growth was followed by a high rate of growth that was approximately three orders faster $\sim(r_b/R)^6$ than during the bridge phase ($r_b/R \lesssim 1$) and reached a maximum at $r_b/R = 2^{1/3}$. This large increase in p_y^+ corresponds to the entirely positive radial flow observed in Figure 3f. Beyond this point in our simulations, p_y^+ began to decay due to the inherent symmetry of the simulated system with energy being stored in the stretched interface as the momentum of the flow carried the bridge radius past the final equilibrium position of $r_b/R = 2^{1/3}$. However, due to the breaking of symmetry by the condensing surface, in our experiments this excess momentum at $r_b/R = 2^{1/3}$ is unbalanced and can contribute directly to the momentum of the jumping droplet. Note that, for the analysis performed here, we have defined the excess momentum as the maximum momentum at $r_b/R \geq 2^{1/3}$. This provides consistency for the situation where the peak in momentum may occur at $r_b/R < 2^{1/3}$ for *Oh* numbers larger than those simulated here and in the viscous limit ($r_c/R \gtrsim 1$) where we expect all momentum in the system to tend to zero as $r_b/R \rightarrow 2^{1/3}$.

As *Oh* was increased in the simulations, the momentum growth rate in the bridge phase slowed down and the characteristic kink in momentum growth beyond $r_b/R = 1$ observed for smaller *Oh* (= 0.012) was smoothed out. This corresponded with a reduction in the excess momentum obtained at $r_b/R \approx 2^{1/3}$ and a shift to smaller values of r_b/R where the maximum momentum occurred. In the p_y^- region, the minimum found at $r_b/R \approx 1$ for low *Oh* shifted to smaller values of r_b/R and decreased in magnitude. The change in momentum generated with increasing *Oh* is consistent with the coalescence dynamics moving into the transition region between the inertially and viscously dominated coalescence regimes as $r_c/R \rightarrow 1$.[35]

To complete the picture of flow momentum available for droplet jumping, we considered the lower region of the coalescing droplets ($y < 0$) where the sign of the momentum components are reversed. Distinct from the upper region ($y > 0$), the bridging flow interacts with the condensing surface. At the moment when the bridge impacts the surface ($r_b/R \approx 1$), the flow in the negative *y*-direction has a momentum $-p_y^+|_{r_b/R=1}$. The bridge impact develops a region of high pressure as the dynamic pressure of the flow is converted to static pressure,[1] imposing a force on the liquid and the interface. For simplicity, we assumed that the flow momentum induced by this pressure is equal, but opposite, to the momentum in the negative *y*-direction just prior to impact, $p_y^+|_{r_b/R=1}$. We also considered the contribution to the *y*-component of momentum of the internal flow in the flow neighboring the bridge, $-p_y^-|_{r_b/R=1}$. While detailed analysis of 3D simulations are required to confirm these assumptions, we can bound the momentum available for jumping by $p_y^+|_{\max(r_b/R \geq 2^{1/3})}$ and $2p_y^+|_{\max(r_b/R \geq 2^{1/3})}$. Verification that the experimental data lay between these bounds will support our developed approach, with the specific expression derived below as a starting point for a more complex description of the full three-dimensional dynamics.

Next, we balanced the *y*-momentum of the coalescing droplet system by summing the three identified *y*-components of momentum generated by the internal flow and compared them to the total momentum of the jumping droplet,

$$\sum p_y/(m_j U) = (p_y^+|_{r_b/R=1} + p_y^+|_{\max(r_b/R \geq 2^{1/3})} - p_y^-|_{r_b/R=1})/(m_j U) = \frac{v_j}{U} \quad (6)$$

In Figure 5d, $p_y^+|_{\max(r_b/R \geq 2^{1/3})}/(m_j U)$ and the summation of contributing momentum *y*-components given by eq 6 are plotted as a function of the *Oh* number. As *Oh* increases, there is an approximately linear decrease in available internal flow momentum for droplet jumping ($\Sigma p_y(m_j U) \sim -Oh$), resulting in an approximately 2× reduction in dimensionless jumping velocity as *Oh* increases from 0.01 to 0.12. In addition, the $p_y^+|_{\max(r_b/R \geq 2^{1/3})}/(m_j U)$ term contributes two-thirds of the momentum to the jumping process, ≈67%, over the range of *Oh* simulated (see Figure 5d and Supporting Information S8) with the remainder of the contributing momentum originating from the bridge impact region.[1] A fit to the numerical data resulted in the following expression for the jumping velocity

$$v_j = (3.4026Oh^2 - 1.5285Oh + 0.2831)U \quad (7)$$

(see Supporting Information S9 for fit statistics). Toward the inviscid limit ($Oh \rightarrow 0$), the jumping velocity is $v_j \approx 0.28U$. When we calculate the kinetic energy of the jumping droplet based on this velocity and compare to the available excess surface energy in the system (ΔE), only ≈6% of the excess surface energy budget was converted to the translational kinetic energy of the jumping droplet (E_j). As *Oh* increased, the energy conversion efficiency ($\eta_j = E_j/\Delta E$) decreased further reaching $\eta_j \approx 1.8\%$ for $Oh = 0.12$ (see Supporting Information S10). Interestingly, the conversion efficiencies of coalescence-induced droplet jumping are

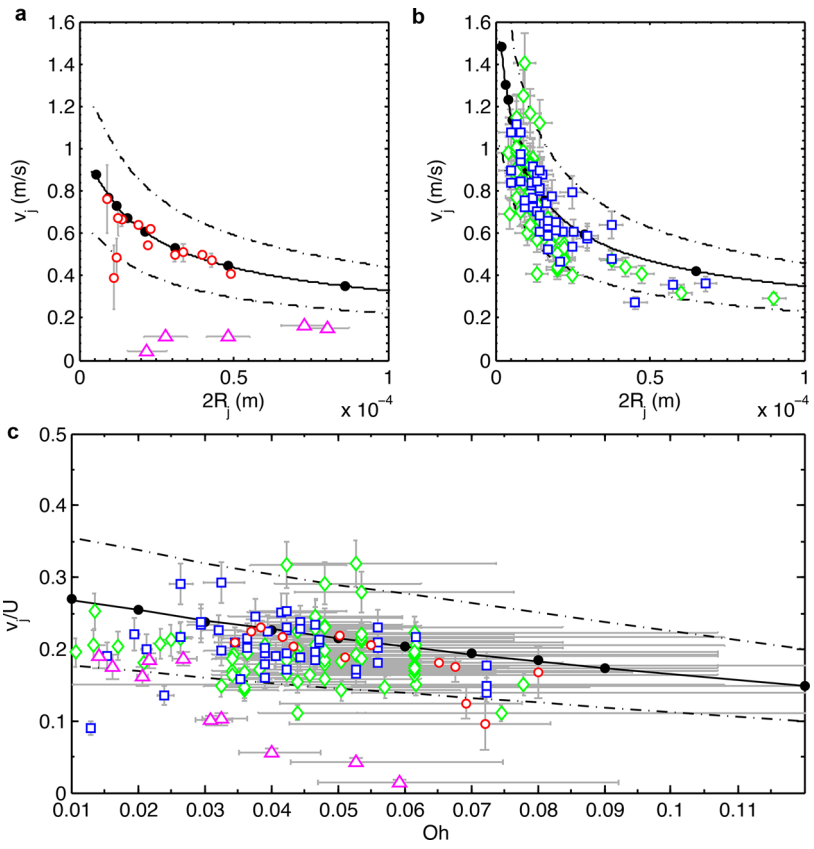

Figure 6. Comparison of experimental data to numerical predictions. Jumping velocities as a function of jumping droplet diameter for (a) the two-camera arrangement and (b) the one-camera arrangement with properties evaluated at (a) T_w = 5 °C and (b) T_w = 26 °C to correspond with the experimental conditions. The dimensionless jumping velocity is plotted as a function of *Oh* in (c). In (a), the open circles are the data from the two-camera arrangement for the P2i−CNT surface and the open triangles are the data from ref 7. In (b), the squares and diamonds are the data from the one-camera arrangement for the P2i−CNT and P2i−CuO surfaces, respectively. In (a−c), the closed circles show the prediction of the numerical simulations (Figure 5d) and the solid line is given by eq 7. The dot-dashed lines in (a−c) represent the bounds of $p_y^+|_{\max(r_b/R\geq 2^{1/3})}$ and $2p_y^+|_{\max(r_b/R\geq 2^{1/3})}$.

characteristically smaller than those of a solid disc transitioning to a sphere as it melts, where $\eta_j \approx 20\%$ has been found.[17] This characteristically larger η_j further highlights the importance of the internal flow momentum developed during the capillary-driven jumping process, which is intimately linked to the initial geometry of the system. Next, we compared the results of the numerical simulations to the experimentally measured jumping velocities.

Comparison to Experiment. In Figure 6a,b, our experimentally measured droplet jumping velocities and the predictions of our numerical simulations (eq 6 and Figure 5d) are plotted as a function of the jumping droplet diameter, $2R_j$. Also shown in Figure 6a is a previously obtained experimental data set.[7] For experiments performed under low pressure in the environmental chamber (Figure 6b), where vapor density was reduced, but viscosity remained approximately unchanged such that the Reynolds number was small ($Re \leq 1$), a simple linear fit was applied to the measured droplet trajectory to determine the jumping speed due to the potential for molecular slip effects on the drag force. Unlike the two-camera arrangement (Figure 6a), the initial conditions before coalescence were difficult to ascertain using a single-camera arrangement (Figure 6b), especially with decreasing droplet radii. However, we classified jumping events based on the angular deviation of the droplet trajectories from the surface normal, rejecting jumping events deviating more than 5° from the normal. Also rejected from the analysis were droplet jumping events triggered by incoming droplets (see Supporting Information S1 for movie details).[7,9] In general, data obtained from the one-camera arrangement showed more scatter due to our inability to completely filter coalescing droplets with nonequal radii and jumping events triggered by more than two droplets.

We demonstrated excellent agreement between our numerical predictions and experimental data with the latter well-bounded by the limits placed on the jumping speed by $p_y^+|_{\max(r_b/R\geq 2^{1/3})}$ and $2p_y^+|_{\max(r_b/R\geq 2^{1/3})}$, giving us confidence in our interpretation of the physics. In addition, we found that the data measured using the two-camera arrangement, which removes the ambiguity surrounding the initial coalescence conditions associated with the one-camera arrangement, followed the numerical predictions exceptionally well. Indeed, for the

experiment presented in Figure 2 using the two-camera arrangement, the numerical simulations predicted $v_j = 0.23U$, which was within 10% of the experimental jumping velocity of $v_j \approx 0.21U$. For the one-camera arrangement, we measured jumping speeds as high as 1.4 m/s, approximately six times larger than previously reported,[7] due to a combination of the elevated temperature of the environmental chamber with respect to ambient and the smaller jumping droplet diameters allowed by our nanostructured surfaces. Experiments performed in the environmental chamber also confirmed that the surrounding gas pressure played no role on the jumping speed (see Supporting Information S11).

Interestingly, previous experimental data are well-captured by our numerical results without the need to introduce a surface adhesion term for $2R_j > 100\ \mu$m,[7] indicating that droplets in this size range had reached a constant contact angle growth wetting state characterized by macroscopic contact angle measurements on this surface, $\theta \approx 170°$, $\Delta\theta \approx 0°$.[42] However, for droplets smaller than 100 μm, there was an increasing discrepancy in comparison to our numerical results. While it has previously been suggested that the observed peak and then decreasing jumping speed with decreasing droplet size arises as a result of internal viscous dissipation,[7,9,13,43] the jumping speeds fall off faster than our experimental and numerical data in this range of *Oh* (Figure 6c). This observation implicates a surface interaction mechanism rather than a fundamental hydrodynamic limitation and highlights that the details of the evolving droplet morphology need to be carefully considered when interpreting experimental data of droplet jumping. Indeed, complex wetting interactions associated with condensed droplet growth on hierarchical surfaces have been shown to influence the ability of coalescing droplets to jump,[10] a fact not captured in our present analysis. However, we believe that the mechanistic framework we have developed to understand droplet jumping can be readily extended to deal with these nonidealities.

CONCLUSIONS

In summary, we demonstrated experimentally and numerically that coalescence-induced droplet jumping on ultra-low adhesion surfaces is fundamentally inefficient. Through the use of detailed measurements of jumping droplets during water condensation coupled with numerical simulations of binary droplet coalescence, we have elucidated that only a small fraction of the excess surface energy ($\leq$6%) is convertible into translational kinetic energy. These findings clarify the role of internal fluid dynamics during the jumping droplet coalescence process and underpin the development of systems that can harness jumping droplets for a wide range of applications. Furthermore, this work offers fundamentally new insight into the process of coalescence-induced droplet jumping and has defined a fundamental upper bound for jumping speeds on flat nonwetting surfaces.

METHODS

Surface Synthesis. Carbon nanotubes were grown by chemical vapor deposition (CVD).[44] Silicon growth substrates were prepared by sequentially depositing a 20 nm thick Al_2O_3 diffusion barrier and a 5 nm thick film of Fe catalyst layer using electron-beam deposition. Growth was performed in a 2.54 cm quartz furnace tube. Following a 15 min purge in a H_2/He atmosphere, the growth substrate was annealed by ramping the furnace temperature to 750 °C followed by a 3 min anneal at temperature, while maintaining a flow of H_2 and He at 400 and 100 sccm, respectively. CNT growth was then initiated by flowing C_2H_4 at 200 sccm. The flow of C_2H_4 was stopped after a period of 1 min. The thermally grown CNT had a typical outer diameter of $d \approx 7$ nm. Due to the short growth time ($\sim$5 min), the CNT did not form a well-aligned forest, but rather a tangled turf.

To create the CuO nanostructures, commercially available oxygen-free Cu tabs (20 mm × 2 mm × 1 mm) were used (99.9% purity), as the test samples for the experiments. Each Cu tab was cleaned in an ultrasonic bath with acetone for 10 min and rinsed with ethanol, isopropyl alcohol and deionized (DI) water. The tabs were then dipped into a 2.0 M hydrochloric acid solution for 10 min to remove the native oxide film on the surface, then triple-rinsed with DI water and dried with clean nitrogen gas. Nanostructured CuO films were formed by immersing the cleaned tabs into a hot (96 ± 3 °C) alkaline solution composed of $NaClO_2$, NaOH, $Na_3PO_4 \cdot 12H_2O$, and DI water (3.75:5:10:100 wt %).[45] During the oxidation process, a thin ($\approx$300 nm) Cu_2O layer was formed that then reoxidized to form sharp, knife-like CuO oxide structures with heights of $h \approx 1\ \mu$m, solid fraction $\varphi \approx 0.023$ and roughness factor $r \approx 10$.

To functionalize the surfaces, a proprietary fluorinated polymer was deposited using plasma enhanced vapor deposition (P2i). The process occurs under low pressure within a vacuum chamber at room temperature. The coating is introduced as a vapor and ionized. This process allows for the development of a highly conformal ($\approx$30 nm thick) polymer layer, which forms a covalent bond with the surface, making it extremely durable. Goniometric measurements (MCA-3, Kyowa Interface Science Ltd.) of $\approx$100 nL droplets on a smooth P2i coated silicon wafer surface showed advancing and receding contact angles of $\theta_a = 124.3° \pm 3.1°$ and $\theta_r = 112.6° \pm 2.8°$, respectively. Using the values of the advancing angles on the rough and smooth P2i surfaces, we estimated the effective solid fraction of both the CNT and CuO surfaces to be $\varphi = (\cos\theta_a^{app} + 1)/(\cos\theta_a + 1) \approx 0.03$.

Jumping Droplet Experiments. Condensation experiments carried out under humid atmospheric conditions used two cameras that were orthogonally aligned and focused at the same point in space (MCA-3, Kyowa Interface Science Ltd.) (see Supporting Information S2). An overhead CCD camera was used to capture images of the droplets prior to coalescence to provide the initial conditions. The out-of-plane trajectory of the jumping droplets was captured using a high-speed camera (Fastcam SA2, Photron) at frame capture rates of 5, 7.5, and 18 kHz corresponding to shutter speeds of 185, 133, and 56 μs, respectively. Back illumination was provided by a fiber light positioned behind the sample with respect to the high-speed camera. The experiment was initiated by first cooling the surface to a temperature of $T_w = 5$ °C, corresponding to a local saturation pressure of $p_w = 0.9$ kPa on a cold-stage under a dry N_2 stream. The dry N_2 stream was then shut-off to initiate condensation from

the ambient atmosphere with a relative humidity of ≈55% and a dry-bulb temperature of ≈20 °C corresponding to a vapor saturation pressure of $p_v \approx 1.28$ kPa and a supersaturation of $S = p_v/p_w \approx 1.42$.

Condensation experiments were also carried out under saturated conditions in a pressure regulated environmental chamber using a single-camera arrangement (see Supporting Information S3 and S4). The out-of-plane trajectory of the jumping droplets was captured using a high-speed camera (Phantom v7.1, Vision Research) at frame capture rates of 7.2, 10, and 20 kHz corresponding to shutter speeds of 139, 100, and 50 μs, respectively. The camera was mounted outside of the environmental chamber and fitted with an extended macro lens assembly. Illumination was supplied by light emitting diodes installed inside the chamber and providing back lighting to the sample. The sample tabs were mounted to a flattened copper tube connected to an external cooling loop and was maintained at a temperature of $T_w = 26$ °C ($p_w = 3.33$ kPa). The water vapor supply was vigorously boiled before the experiments to remove noncondensable gases. The experiment was initiated by first evacuating the environmental chamber to medium-vacuum levels (=0.5 ± 0.025 Pa). Water vapor was then introduced into the environmental chamber *via* a bellows valve set to maintain the chamber pressure at $p_v = 3.6 \pm 0.175$ kPa corresponding to a supersaturation of $S \approx 1.05$.

Numerical Modeling. A purpose-built finite-element-based computational code was used to capture the dynamics of the coalescence process. The bulk flow of the liquid is governed by the incompressible Navier−Stokes equations, while the boundary conditions are given by either the conventional model or by the interface formation model, which generalizes the usual boundary conditions for flows in which interfaces are formed or destroyed.[46] In the range of parameter space studied in this paper, the differences in the predictions of the two models for the global dynamics of the drops was small; however, larger differences may be expected when considering smaller drops.

A full description of the models used, benchmark simulations confirming the codes accuracy and a comparison to recent experimental data are provided in ref 40. Furthermore, a step-by-step user-friendly guide to the development of the code can be found in ref [47] and the extension to interface formation dynamics is in ref 41. Therefore, here we only briefly recapitulate the main details.

The code uses an arbitrary Lagrangian Eulerian approach, so that the free surface dynamics are captured with high accuracy. The mesh is based on the bipolar coordinate system, and is graded so that exceptionally small elements can be placed near the bridge front; consequently, in contrast to many previous works, both local and global physical scales of the coalescence process are properly resolved. Triangular finite elements of V6P3 type are used and the result of our spatial discretization is a system of nonlinear differential algebraic equations of index two, which are solved using the second-order backward differentiation formula using a time step, which automatically adapts during a simulation to capture the appropriate temporal scale at that instant.

Conflict of Interest: The authors declare no competing financial interest.

Acknowledgment. Bell Labs Ireland thanks the Industrial Development Agency (IDA) Ireland for their financial support. R.E. acknowledges funding received from the Irish Research Council for Science, Engineering, and Technology, cofunded by Marie Curie Actions under FP7. R.E., N.M., and E.N.W. gratefully acknowledge funding support from the MIT S3TEC Center, an Energy Frontier Research Center funded by the Department of Energy, Office of Science, Basic Energy Sciences under Award No. DE-FG02-09ER46577, and the Office of Naval Research (ONR) with Dr. Mark Spector as program manager. R.E., N.M., and E.N.W. also acknowledge the support from the National Science Foundation through the Major Research Instrumentation Grant for Rapid Response Research (MRI-RAPID) for the microgoniometer. We acknowledge support from P2i for the hydrophobic layer depositions. A portion of this work was performed in part at the Center for Nanoscale Systems (CNS), a member of the National Nanotechnology Infrastructure Network (NNIN), which is supported by the National Science Foundation under NSF Award No. ECS-0335765. CNS is part of Harvard University. Any opinion, findings, and conclusions or recommendations expressed in this material are those of the authors(s) and do not necessarily reflect the views of the National Science Foundation.

Supporting Information Available: One video (.mov) showing incoming droplet triggered jumping, as well as further information on the jumping-droplet experiments, data collection methodology, and supplementary analysis. This material is available free of charge *via* the Internet at http://pubs.acs.org.

REFERENCES AND NOTES

1. Nam, Y. S.; Kim, H.; Shin, S. Energy and Hydrodynamics Analyses of Coalescence-Induced Jumping Droplets. *Appl. Phys. Lett.* **2013**, *103*, 161601.
2. Miljkovic, N.; Enright, R.; Nam, Y.; Lopez, K.; Dou, N.; Sack, J.; Wang, E. N. Jumping-Droplet-Enhanced Condensation on Scalable Superhydrophobic Nanostructured Surfaces. *Nano Lett.* **2012**, *13*, 179–187.
3. Miljkovic, N.; Preston, D.; Enright, R.; Wang, E. N. Electrostatic Charging of Jumping Droplets. *Nat. Commun.* **2013**, *4*, 251710.1038/ncomms3517.
4. Enright, R.; Miljkovic, N.; Dou, N.; Nam, Y.; Wang, E. N. Condensation on Superhydrophobic Copper Oxide Nanostructures. *J. Heat Transfer* **2013**, *135*, 091304.
5. Enright, R.; Miljkovic, N.; Al-Obeidi, A.; Thompson, C. V.; Wang, E. N. Condensation on Superhydrophobic Surfaces: The Role of Local Energy Barriers and Structure Length Scale. *Langmuir* **2012**, *28*, 14424–14432.
6. Boreyko, J. B.; Collier, C. P. Delayed Frost Growth on Jumping-Drop Superhydrophobic Surfaces. *ACS Nano* **2013**, *7*, 1618–1627.
7. Boreyko, J. B.; Chen, C. H. Self-Propelled Dropwise Condensate on Superhydrophobic Surfaces. *Phys. Rev. Lett.* **2009**, *103*, 184501.
8. Boreyko, J. B.; Chen, C. H. Self-Propelled Jumping Drops on Superhydrophobic Surfaces. *Phys. Fluids* **2010**, *22*, 091110.
9. Lv, C.; Hao, P.; Yao, Z.; Song, Y.; Zhang, X.; He, F. Condensation and Jumping Relay of Droplets on Lotus Leaf. *Appl. Phys. Lett.* **2013**, *103*, 021601.
10. Rykaczewski, K.; Paxson, A. T.; Anand, S.; Chen, X.; Wang, Z.; Varanasi, K. K. Multimode Multidrop Serial Coalescence Effects During Condensation on Hierarchical Superhydrophobic Surfaces. *Langmuir* **2012**, *29*, 881–891.
11. He, M.; Zhou, X.; Zeng, X.; Cui, D.; Zhang, Q.; Chen, J.; Li, H.; Wang, J.; Cao, Z.; Song, Y.; *et al.* Hierarchically Structured Porous Aluminium Surfaces for High-Efficient Removal of Condensed Water. *Soft Matter* **2012**, *8*, 6680–6683.
12. He, M.; Zhang, Q.; Zeng, X.; Cui, D.; Chen, J.; Li, H.; Wang, J.; Song, Y. Hierarchical Porous Surface for Efficiently Controlling Microdroplets' Self-Removal. *Adv. Mater.* **2013**, *25*, 2291–2295.
13. Wang, F.-C.; Yang, F.; Zhao, Y.-P. Size Effect on the Coalescence-Induced Self-Propelled Droplet. *Appl. Phys. Lett.* **2011**, *98*, 053112.
14. Chen, X.; W, J. Nanograssed Micropyramidal Architectures for Continuous Dropwise Condensation. *Adv. Funct. Mater.* **2011**, *21*, 4617–4623.
15. Feng, J.; Qin, Z.; Yao, S. Factors Affecting the Spontaneous Motion of Condensate Drops on Superhydrophobic Copper Surfaces. *Langmuir* **2012**, *28*, 6067–6075.
16. Peng, B.; Wang, S.; Lan, Z.; Xu, W.; Wen, R.; Ma, X. Analysis of Droplet Jumping Phenomenon with Lattice Boltzmann Simulation of Droplet Coalescence. *Appl. Phys. Lett.* **2013**, *102*, 151601.
17. Habenicht, A.; Olapinski, M.; Burmeister, F.; Leiderer, P.; Boneberg, J. Jumping Nanodroplets. *Science* **2005**, *309*, 2043–2045.
18. Lee, S.; Lee, S.; Kang, K. Jumping of a Droplet on a Superhydrophobic Surface in AC Electrowetting. *J. Visualization* **2011**, *14*, 259–264.
19. Jun Lee, S.; Lee, S.; Hyoung Kang, K. Droplet Jumping by Electrowetting and Its Application to the Three-Dimensional Digital Microfluidics. *Appl. Phys. Lett.* **2012**, *100*, 081604.

20. Mockenhaupt, B.; Ensikat, H.-J.; Spaeth, M.; Barthlott, W. Superhydrophobicity of Biological and Technical Surfaces Under Moisture Condensation: Stability in Relation to Surface Structure. *Langmuir* **2008**, *24*, 13591–13597.
21. Miljkovic, N.; Preston, D. J.; Enright, R.; Wang, E. N. Electric-Field-Enhanced Condensation on Superhydrophobic Nanostructured Surfaces. *ACS Nano* **2013**, *7*, 11043–11054.
22. Miljkovic, N.; Wang, E. N. Condensation Heat Transfer on Superhydrophobic Surfaces. *MRS Bull.* **2013**, *38*, 397–406.
23. Enright, R.; Miljkovic, N.; Alvarado, J. L.; Kim, K.; Rose, J. W. Dropwise Condensation on Micro- and Nanostructured Surfaces. *Nanoscale Microscale Thermophys. Eng.* **2014**, *18*, 223–250.
24. Wisdom, K. M.; Watson, J. A.; Qu, X.; Liu, F.; Watson, G. S.; Chen, C.-H. Self-Cleaning of Superhydrophobic Surfaces by Self-Propelled Jumping Condensate. *Proc. Natl. Acad. Sci. U.S.A.* **2013**, *110*, 7992–7997.
25. Boreyko, J. B.; Zhao, Y.; Chen, C. H. Planar Jumping-Drop Thermal Diodes. *Appl. Phys. Lett.* **2011**, *99*, 234105.
26. Boreyko, J. B.; Chen, C.-H. Vapor Chambers with Jumping-Drop Liquid Return from Superhydrophobic Condensers. *Int. J. Heat Mass Transfer* **2013**, *61*, 409–418.
27. Zhang, Q.; He, M.; Chen, J.; Wang, J.; Song, Y.; Jiang, L. Anti-Icing Surfaces Based on Enhanced Self-Propelled Jumping of Condensed Water Microdroplets. *Chem. Commun.* **2013**, *49*, 4516–4518.
28. Chen, X.; Ma, R.; Zhou, H.; Zhou, X.; Che, L.; Yao, S.; Wang, Z. Activating the Microscale Edge Effect in a Hierarchical Surface for Frosting Suppression and Defrosting Promotion. *Sci. Rep.* **2013**, *3*, 251510.1038/srep02515.
29. Miljkovic, N.; Preston, D. J.; Enright, R.; Wang, E. N. Jumping-Droplet Electrostatic Energy Harvesting. *Appl. Phys. Lett.* **2014**, *105*, 013111.
30. Khawaji, A. D.; Kutubkhanah, I. K.; Wie, J. M. Advances in Seawater Desalination Technologies. *Desalination* **2008**, *221*, 47–69.
31. Foresti, D.; Nabavi, M.; Klingauf, M.; Ferrari, A.; Poulikakos, D. Acoustophoretic Contactless Transport and Handling of Matter in Air. *Proc. Natl. Acad. Sci. U.S.A.* **2013**, 12549–1255410.1073/pnas.1301860110.
32. Jaworek, A.; Krupa, A.; Sobczyk, A. T.; Marchewicz, A.; Szudyga, M.; Antes, T.; Balachandran, W.; Di Natale, F.; Carotenuto, C. Submicron Particles Removal by Charged Sprays. Fundamentals. *J. Electrost.* **2013**, *71*, 345–350.
33. Kollera, M.; Grigull, U. Uber das Abspringen von Tropfen bei der Kondensation von Quecksilber. *Waerme–Stoffuebertrag.* **1969**, *2*, 31–35.
34. Paulsen, J. D.; Burton, J. C.; Nagel, S. R.; Appathurai, S.; Harris, M. T.; Basaran, O. A. The Inexorable Resistance of Inertia Determines the Initial Regime of Drop Coalescence. *Proc. Natl. Acad. Sci. U.S.A.* **2012**, *109*, 6857–6861.
35. Paulsen, J. D.; Burton, J. C.; Nagel, S. R. Viscous to Inertial Crossover in Liquid Drop Coalescence. *Phys. Rev. Lett.* **2011**, *106*, 114501.
36. Duchemin, L.; Eggers, J.; Josserand, C. Inviscid Coalescence of Drops. *J. Fluid Mech.* **2003**, *487*, 167–178.
37. Thoroddsen, S. T.; Takehara, K.; Etoh, T. G. The Coalescence Speed of a Pendent and Sessile Drop. *J. Fluid Mech.* **2005**, *527*, 85–114.
38. Wu, M.; Cubaud, T.; Ho, C.-M. Scaling Law in Liquid Drop Coalescence Driven by Surface Tension. *Phys. Fluids* **2004**, *16*, L51–L54.
39. Eggers, J.; Lister, J. R.; Stone, H. A. Coalescence of Liquid Drops. *J. Fluid Mech.* **1999**, *401*, 293–310.
40. Sprittles, J. E.; Shikhmurzaev, Y. D. Coalescence of Liquid Drops: Different Models *versus* Experiment. *Phys. Fluids* **2012**, *24*, 122105.
41. Sprittles, J. E.; Shikhmurzaev, Y. D. Finite Element Simulation of Dynamic Wetting Flows as an Interface Formation Process. *J. Comput. Phys.* **2013**, *233*, 34–65.
42. Boreyko, J. B.; Baker, C. H.; Poley, C. R.; Chen, C.-H. Wetting and Dewetting Transitions on Hierarchical Superhydrophobic Surfaces. *Langmuir* **2011**, *27*, 7502–7509.
43. Liu, T. Q.; Sun, W.; Sun, X. Y.; Ai, H. R. Mechanism Study of Condensed Drops Jumping on Super-Hydrophobic Surfaces. *Colloids Surf., A* **2012**, *414*, 366–374.
44. Hart, A. J.; Slocum, A. H. Rapid Growth and Flow-Mediated Nucleation of Millimeter-Scale Aligned Carbon Nanotube Structures from a Thin-Film Catalyst. *J. Phys. Chem. B* **2006**, *110*, 8250–8257.
45. Nam, Y.; Sungtaek, Y. A Comparitive Study of the Morphology and Wetting Characteristics of Micro/Nanostructured Cu Surfaces for Phase Change Heat Transfer Applications. *J. Adhes. Sci. Technol.* **2013**, *27*, 2163–2176.
46. Shikhmurzaev, Y. D. *Capillary Flows with Forming Interfaces*; CRC Press: Boca Raton, FL, 2007.
47. Sprittles, J. E.; Shikhmurzaev, Y. D. Finite Element Framework for Describing Dynamic Wetting Phenomena. *Int. J. Numer. Methods Fluids* **2012**, *68*, 1257–1298.